Biomass and Bioenergy 184 (2024) 107197

Contents lists available at ScienceDirect

Biomass and Bioenergy

journal homepage: www.elsevier.com/locate/biombioe

Enhancing waste hemp hurd-derived anodes for sodium-ion batteries through hydrochloric acid-mediated hydrothermal pretreatment

Daniel Antorán [a,b], Darío Alvira [a,b], Víctor Sebastián [b,c,d], Joan J. Manyà [a,b,*]

[a] Aragón Institute for Engineering Research (I3A), Thermochemical Processes Group, University of Zaragoza, Escuela Politécnica Superior, Crta. de Cuarte s/n, 22071, Huesca, Spain
[b] Department of Chemical Engineering and Environmental Technologies, University of Zaragoza, Campus Río Ebro, María de Luna 3, 50018, Zaragoza, Spain
[c] Aragón Institute of Nanoscience and Materials (INMA), CSIC-University of Zaragoza, Campus Río Ebro, Edificio I+D, Mariano Esquillor s/n, 50018, Zaragoza, Spain
[d] Networking Research Center on Bioengineering, Biomaterials and Nanomedicine, CIBER-BBN, 28029, Madrid, Spain

ARTICLE INFO

Keywords:
Sodium-ion battery
Hard carbon
Waste hemp hurd
Acid-mediated hydrothermal pretreatment
Rate capability

ABSTRACT

Waste hemp hurd (WHH) was used as a sustainable feedstock for producing hard carbon-based anodes for sodium-ion batteries (SIBs). Two easily scalable production pathways were tested and compared: (1) pyrolysis (at 500 °C) and subsequent annealing at 800, 1000 or 1200 °C, and (2) hydrothermal pretreatment (at 180 °C) and subsequent annealing at the above-mentioned highest temperatures. Results indicated that when a HCl (2 mol m^{-3}) aqueous solution was used as hydrothermal medium, the textural, structural and surface chemistry features linked to the electrochemical performance of the resulting hard carbons improved. The WHH-derived electrode produced via HCl-mediated hydrothermal pretreatment and subsequent annealing at 1000 °C showed an exceptional electrochemical performance in terms of specific capacity (535 mA h g^{-1} at 30 mA g^{-1}) and rate capability (372, 156, 115, and 83 mA h g^{-1} at 0.1, 0.5, 1, and 2 A g^{-1}, respectively) when an ester-based electrolyte was used (NaTFSI in EC/DMC). Using an ether-based electrolyte ($NaPF_6$ in diglyme) improved both the ICE (from 69% to 78%) and cycling stability (85% of capacity retention after 300 cycles at 1 A g^{-1}; 91% when current rate returned to 0.1 A g^{-1}). In summary, relatively low-cost WHH-derived carbons are able to deliver an exceptional performance, much better than that reported so far for other biomass-derived carbons, and even close to that exhibited by more expensive and complex composite and hybrid materials.

1. Introduction

Electrochemical energy storage (EES) is crucial to smooth the intermittency of renewable electricity generation in the carbon-neutral future. A globally installed storage capacity of more than 1 TWh in batteries is foreseen for 2030 [1]. This massive expansion of storage capacity leads to great challenges not only with respect to energy and power densities, but also regarding additional aspects such as the sustainability and availability of raw materials. In this context, alternative technologies to the state-of-the-art lithium-ion batteries are needed.

Sodium-ion batteries (SIBs) appear as one of the most promising postlithium chemistry due to their relatively low cost, abundance and wide distribution of sodium, as well as their chemical similarities to LIBs [2]. Nevertheless, the main challenge for SIBs still lies in the development of high-performance and sustainable electrode materials toward industrially relevant EES devices. For the negative electrode, graphite, which is commonly used as anode in LIBs, shows a very limited sodium-ion storage capacity (ca. 35 mA h g^{-1}) when carbonates-based electrolytes are used. This has been attributed to the thermodynamic instability of the binary Na-intercalated graphite compound [3]. Recently, it has been reported that using ether-based electrolytes enables graphite to reversibly accommodate Na^+ via co-intercalation reactions, where solvated alkali ions are intercalated into the galleries of graphite through a ternary graphite intercalation compound [4,5]. However, the non-renewable nature and global supply risk of natural graphite has led to increased interest in hard carbons (HCs), which can be obtained from biomass, therefore, contributing to simultaneously replace fossil-based resources and boost circular bioeconomy.

HCs possess a highly disordered structure with large interlayer space (d_{002}) and defects, as well as a number of micropores that are located

* Corresponding author. Aragón Institute for Engineering Research (I3A), Thermochemical Processes Group, University of Zaragoza, Escuela Politécnica Superior, Crta. de Cuarte s/n, 22071, Huesca, Spain.
E-mail address: joanjoma@unizar.es (J.J. Manyà).

https://doi.org/10.1016/j.biombioe.2024.107197
Received 30 January 2024; Received in revised form 22 March 2024; Accepted 22 March 2024
Available online 28 March 2024
0961-9534/© 2024 The Authors. Published by Elsevier Ltd. This is an open access article under the CC BY-NC-ND license (http://creativecommons.org/licenses/by-nc-nd/4.0/).

between these structures [6]. Insertion of Na^+ into HCs mainly occurs in two stages during galvanostatic discharge: a so-called slope region at relatively high voltage (above 0.15 V) and a plateau region at low voltage (below 0.15 V) [7]. Although the nature of the processes behind the slope and plateau regions is still debated by the research community, there is a growing consensus that the low- and high-voltage regions are mainly ascribed to adsorption-driven storage processes (charge storage on the surface, heteroatoms, and defects) and intercalation and closed pore filling processes, respectively [8]. Nonetheless, HCs still suffer from some issues that limit their applicability, such as low initial Coulombic efficiency (ICE) [9,10], low rate capability, and poorer cycling stability compared to graphitic anodes in LIBs [11,12].

Waste hemp hurd (WHH) is the lignocellulosic residue obtained when bast fibers are separated from industrial hemp stalk. The production of industrial hemp (*Cannabis sativa* L.) in the EU increased by 84% in 2022 compared to 2015 [13]. Since WHH, which is currently used in low added-value applications (e.g., animal bedding, paper products, and building materials), accounts for ca. 50 wt % of the whole plant biomass [14], there is a need to valorize this waste into higher value-added renewable materials. In the field of electrochemical energy storage, only few studies have been reported on the use of WHH as precursor of carbon-based electrodes. Sun et al. observed an excellent electrochemical performance of WHH-derived chemically activated carbons in symmetric supercapacitor cells [15]. Recently, a remarkable rate capability (79 mA h g^{-1} at 1 A g^{-1}) in a sodium-ion half-cell was reported in our previous study for WHH-derived HCs produced through mild chemical activation with K_2CO_3 [16]. This encouraging outcome was mainly ascribed to the unique physicochemical properties of the carbon precursor, since much lower specific capacities at high current rates can be expected for biomass-derived HCs.

On the other hand, hydrothermal pretreatment of carbon precursor has recently been postulated as a key process step to significantly enhance the electrochemical performance of the resulting HCs for SIBs. Xu et al. observed, for glucose-derived HCs, an increased number of active sites in the form of defects and nanovoids when glucose was hydrothermally pretreated [17]. For lignocellulosic precursors, Nieto et al. have also observed a marked improvement of the electrochemical performance (especially at relatively high current rates) of the resulting spent coffee ground-, sunflower seed shell-, and rose stem-derived HCs when the biomass was previously hydrothermally treated up to 250 °C for 24 h under autogenous pressure [18].

It is well known that the addition of strong mineral acids during hydrothermal treatment results in an enhanced removal of ash from nascent hydrochar, as well as a catalyzed hydrolysis and dehydration due to a higher concentration of H^+ in the reaction system [19]. Recently, hydrochloric acid (HCl) has been proven to be effective to overcome the agglomeration of hydrochar, leading to the formation of carbon microspheres when bamboo was hydrothermally processed at 220 °C [20]. Porous carbon microspheres represent a very interesting morphology for SIB purposes, since they can shorten the diffusion pathway of both electrolyte and Na ions compared to regular 3D porous HCs [21].

Taking into account all of the above, the specific aim of the present study was to synthesize high-performance WHH-derived anodes for SIBs via an easily scalable process consisting of two consecutive steps: a hydrothermal pretreatment (w/wo HCl addition) and a subsequent carbonization at higher temperature (800, 1000, and 1200 °C) under argon atmosphere. To get insights into the role of the hydrothermal pretreatment on the properties of the resulting HCs, slow pyrolysis of WHH up to 500 °C was also conducted instead of the hydrothermal step. As explained in detail in the following sections, the best-performing WHH-derived HC—the one produced through HCl-assisted hydrothermal pretreatment and subsequent annealing at 1000 °C—exhibited an impressive electrochemical performance, with specific capacities of 535 and 115 mA h g^{-1} at current densities of 0.03 and 1 A g^{-1}, respectively. This outstanding performance for a redox-active metal-free biomass-derived HC can be ascribed to a unique combination of physicochemical properties, leading to a well-balanced contribution from the high-voltage slope and low-voltage plateau regions.

2. Experimental section

2.1. Synthesis of hard carbons

Waste hemp hurd samples were characterized in terms of proximate and elemental analyses, as well as inorganic composition and biomass constituents. More details on the methodology followed for feedstock characterization can be found in a previous publication [16]. For hydrothermal pretreatment, 5 g of WHH (previously sieved to particles below 5 mm) was loaded with 60 mL of deionized water (DI)—or an aqueous HCl solution (2 mol dm^{-3})—into a polytetrafluoroethylene (PTFE)-lined stainless-steel autoclave, which was then heated up to 180 °C. The reactor was held at this temperature for 12 h and then cooled down to room temperature The resulting hydrochar, was then collected through vacuum filtration and dried at 100 °C for 12 h.

Slow pyrolysis of WHH (also sieved to particles below 5 mm) was conducted using a bench-scale fixed-bed reactor, at atmospheric pressure under a continuous flow of nitrogen, at an average heating rate of 5 °C min^{-1}, and at a highest temperature of 500 °C. Details on the pyrolysis reactor and experimental procedure are available elsewhere [22,23].

Both WHH-derived hydrochars and pyrolysis chars (2 g per batch) were subjected to a second carbonization step up to 800, 1000, and 1200 °C using a tubular mullite-made reactor inserted into a high-temperature furnace (Carbolite TF1 16/60/300) under a continuous flow of argon at a heating rate of 5 °C min^{-1}. A soaking time of 2 h at the highest temperature was applied. The resulting WHH-derived HCs were washed with HCl solution (2 mol dm^{-3}) and then with DI water until neutral pH was reached. They were finally dried at 100 °C for 12 h, grounded and sieved to collect particles below 90 μm. The resulting WHH-derived carbons were denoted as *HC-T*, *HTC-T*, and *HTC-T-HCl* for pyrolysis chars, hydrochars, and HCl-mediated hydrochars carbonized at a given highest temperature value (*T*), respectively.

2.2. Physicochemical characterization

Structural properties of produced carbons were investigated through XRD, using an Empyrean instrument from Malvern Panalytical (UK) with Cu-Kα radiation (λ = 0.154 nm), and Raman spectroscopy, using an alpha 300 microscope from WITec (Germany) at 532 nm laser wavelength. The interlayer spacing between graphene layers (d_{002}), the apparent thickness of crystallites along the *c*-axis (L_c), and the apparent width of crystallites along the *a*-axis (L_a) were determined from XRD spectra using the Bragg's law and Scherrer's equation [24]. According to the methodology suggested by Sadezky et al. [25], Raman spectra were deconvoluted into one Gaussian-shaped band (D3, at about 1500 cm^{-1}) and four Lorentzian-shaped bands (G, D1, D2 and D4 at about 1600, 1360, 1620, and 1200 cm^{-1}, respectively) using the Peak Analyzer tool in OriginPro software. The structural analysis was further assessed by the evaluation of HR-TEM images, which were acquired using an image-corrected Titan 80-300 kV system equipped with a SuperTwin objective lens and corrector for the spherical aberration (C_S), allowing a point-to-point resolution of 0.08 nm. The Digitalmicrograph software was used for image processing.

The morphologies of WHH-derived HCs were observed by scanning electron microscopy (SEM) using an Inspect-F50A microscope from FEI (The Netherlands). To investigate the oxygen- and nitrogen-containing functional groups on surface, X-ray photoelectron spectroscopy (XPS) was conducted using an Axis Supra spectrometer from Katros Analytical (UK) equipped with a monochromatic Al-Kα radiation source running at 1486 eV. C 1s, O 1s and N 1s regions were deconvoluted using the CasaXPS software package. Specific surface areas and pore size

distributions were estimated from combined N_2 and CO_2 adsorption isotherms, which were acquired at −196 °C and 0 °C, respectively, using an Autosorb-iQ-XR2 analyzer from Quantachrome Instruments (Germany). Micropore and mesopore volumes were estimated from N_2 adsorption data, whereas ultramicropore volume (for pore sizes below 0.7 nm) was calculated from CO_2 adsorption data. NLDFT models (for slit pore geometry) implemented in the QuadraWin 6.0 software were used.

2.3. Electrochemical measurements

The working electrodes (WE) were fabricated by mixing in aqueous solution the WHH-derived HCs with acetylene black (as conductive agent) and styrene-butadiene rubber (SBR) and sodium carboxymethyl cellulose (Na-CMC)—as binders—in an 80:10:5:5 mass ratio. A homogeneous slurry was obtained by adding DI water under vortex agitation and magnetic stirring. The slurry was then uniformly coated on a high-purity aluminum sheet (current collector) using a baker applicator to obtain a composite electrode of 100 μm thickness. Finally, the resulting

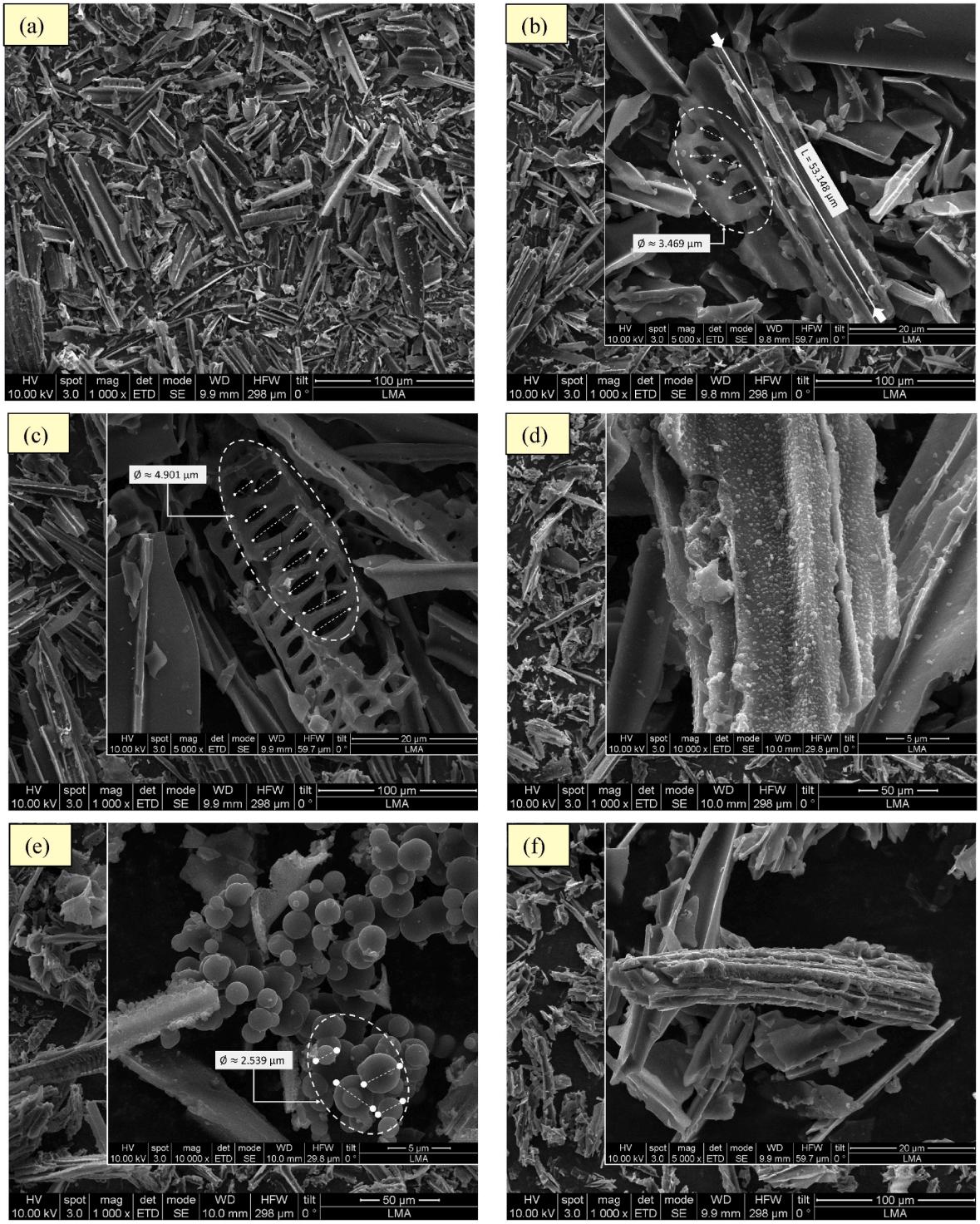

Fig. 1. SEM images of WHH-derived carbons: HC-500 (a), HC-800 (b), HC-1000 (c), HTC-1000 (d), HTC-1000-HCl (e), and HC-1200 (f).

electrodes were punched (12 mm diameter) and dried under vacuum at 120 °C for 12 h. The final mass loading of working electrodes was 1.96 ± 0.34 mg cm^{-2}.

Customized *t*-type Swagelok half-cells were assembled in an Ar-filled glovebox, with O_2 and H_2O contents below 0.5 ppm. More details on the cells can be found in a previous study [26]. The electrolyte (120 μL) was composed of a solution of NaTFSI (1 mol dm^{-3}) in a mixture of EC and DMC (1:1 vol) as solvent. A sodium metal disc (12 mm diameter) was used as counter electrode (CE) and reference electrode (RE) in two-electrode setups, while an additional disc of metal sodium (5 mm diameter) was used as RE in three-electrode cells (see Fig. S1 in supplementary data).

Electrochemical measurements were performed using a potentiostat-galvanostat (model SP-200 from Bio-Logic, France) at room temperature. Galvanostatic discharge/charge (GCD) measurements were conducted within a potential window of 0.01–2.5 V (vs. Na^+/Na), whereas cyclic voltammetry (CV) curves were obtained at a scan rate of 0.1 mV s^{-1} within the same voltage window. Galvanostatic intermittent titration technique (GITT) measurements were also conducted at a constant current density of 0.1 A g^{-1}, a pulse time of 20 min, and relaxation

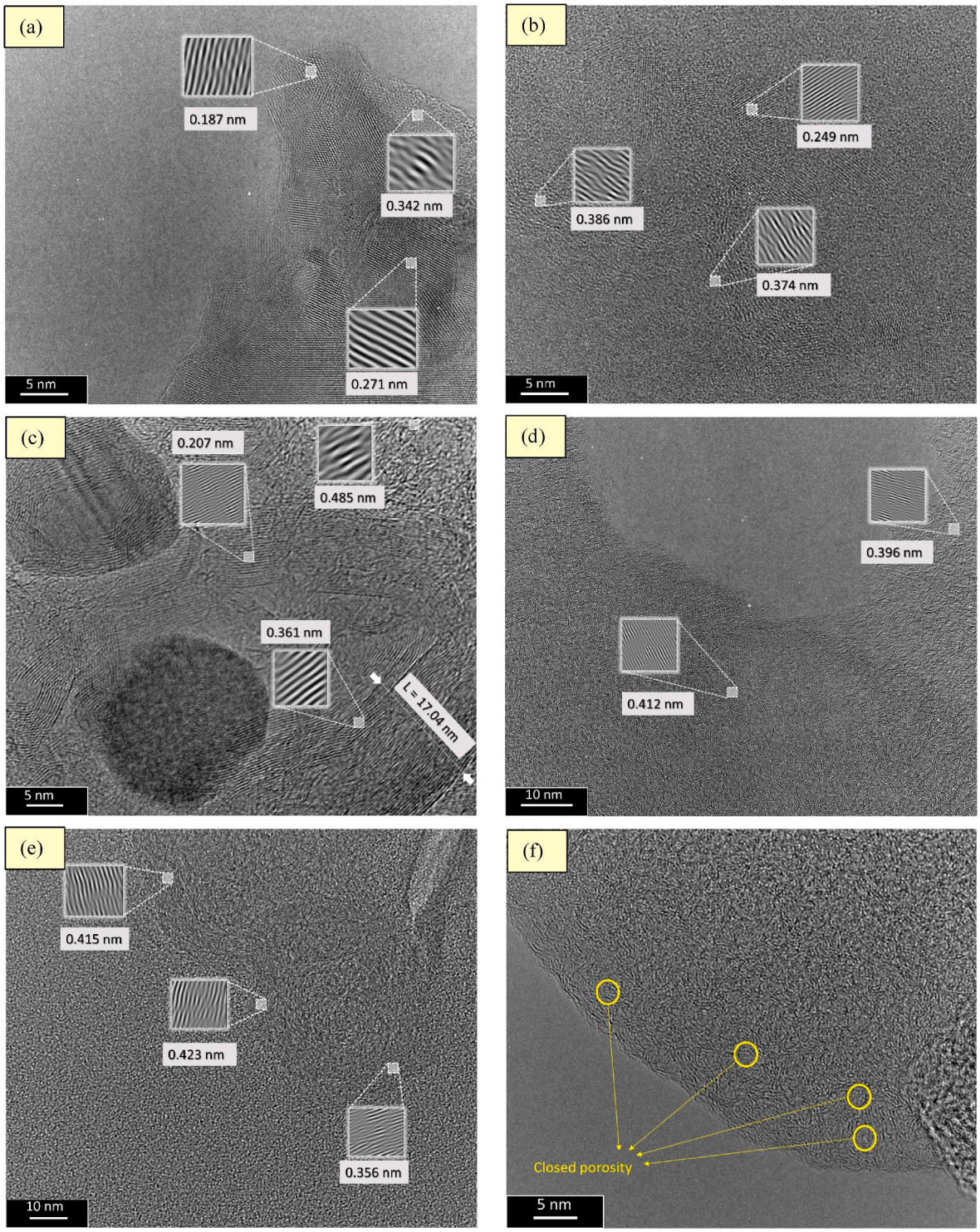

Fig. 2. HR-TEM images of HC-800 (a), HC-1000 (b), HC-1200 (c), HTC-1000 (d), and HTC-1000-HCl (e and f).

periods of 1 h at open circuit. The WE was previously subjected to three CV scans to allow the formation and stabilization of the solid interlayer interphase (SEI).

3. Results and discussion

3.1. Properties of WHH-derived hard carbons

As outlined in our pervious study, in which the same feedstock was used, WHH samples showed well-balanced contents of hemicelluloses, cellulose, and lignin (38.1%, 32.0% and 23.8% respectively in wt. basis), as well as a relatively low ash content (3.0 wt %) [16]. The results from the feedstock characterization are also available in Table S1 (supplementary data).

SEM images of selected WHH derived HCs (as well the intermediate pyrolysis char produced at 500 °C) are given in Fig. 1 (see also Fig. S2 for additional images). It can be seen that all the carbonaceous materials, regardless of the highest carbonization temperature, maintained the fibrous morphology of the biomass precursor. Nevertheless, the hydrothermally pretreated HCs exhibited a considerably rougher surface (see Fig. 1d and e and S2a–d). For HCl-mediated hydrothermal pretreatment, the resulting HCs (especially those carbonized at 1000 °C) showed multiple microspheres (see Fig. 1e) with relatively uniform size (average diameter of ca. 2.5 μm), and moderate degree of aggregation. The resulting interparticle voids between the spheres could provide additional active sites for Na-ion storage.

Fig. 2 shows HR-TEM images of selected carbons—see also Fig. S3 for additional images and their corresponding fast Fourier transform (FFT) patterns—. In general, relatively thin carbon sheets with abundant randomly ordered domains were observed in all cases. For non-hydrothermally pretreated hard carbons, pseudographitic domains with a broad range of interlayer distances were observed (see Fig. 2a, b, and 2c for HC-800, HC-1000, and HC-1200, respectively). For the HC-1200 material, a considerably more ordered structure (especially around the visible macropores) can be seen, probably as a consequence of the deposition of recondensed or repolymerized volatile matter [27,28]. This apparent higher degree of graphitization of HC-1200 is consistent with the more concentric rings observed in the FFT pattern given in Fig. S3. On the other hand, hydrothermally pretreated HCs (regardless of the aqueous medium) showed pseudographitic domains with larger interlayer distances (mostly above the critical value of 0.38 nm suggested in the literature [29]) compared with those observed for HCs produced via pyrolysis and further carbonization (see Fig. 2d and e). Furthermore, relatively large local domains with curved graphene layers surrounding closed (or quasi-closed) pores can be observed in Fig. 2d–f. These microstructures were maintained or even further developed when an acidic medium was used during the hydrothermal pretreatment (see, for instance, Fig. 2f and S3i for HTC-1000-HCl and HTC-1200-HCl, respectively).

With respect to the outcomes of XRD analysis, Fig. S4 shows the acquired XRD patterns. As expected, two broad peaks were observed, with approximate centers at 23° and 44°. The first peak is related to the spacing between graphene layers, whereas the second peak is mostly associated with the contributions of the (100) and (101) reflections [30]. From Table 1, it can be deduced that the d_{002} value was kept almost constant (within the range of 0.38–0.39 nm, which is large enough to ensure Na-ion insertion between the graphene layers) regardless of the production pathway or carbonization temperature. Nevertheless, it should be highlighted that, for all the carbonization temperatures tested in this study, the HCs produced via HCl-assisted hydrothermal pretreatment exhibited the lowest values of L_a (average lateral size), whereas the average thickness of graphene-like layers (L_c) did not differ considerably among the three synthesis processes. XRD results therefore confirm the higher degree of disorder of the resulting hard carbons produced at 1000 and 1200 °C when HCl was used as hydrothermal medium.

Table 1
Structural parameters of WHH-derived carbons deduced from XRD and Raman analyses.

Material	From XRD			From Raman		
	d_{002} (nm)	L_c (nm)	L_a (nm)	A_{D1}/A_G	$A_{D1}/(A_G + A_{D1} + A_{D2})$	FWHM of D1 peak (cm^{-1})
HC-800	0.390	0.940	3.709	4.42 ± 1.08	0.789 ± 0.033	192 ± 6.41
HTC-800	0.388	0.895	3.508	4.79 ± 0.30	0.808 ± 0.001	195 ± 4.77
HTC-800-HCl	0.385	0.880	3.300	4.05 ± 0.55	0.780 ± 0.022	184 ± 3.93
HC-1000	0.381	0.874	4.009	5.22 ± 0.46	0.809 ± 0.013	175 ± 7.07
HTC-1000	0.385	0.968	4.243	5.60 ± 0.16	0.812 ± 0.006	173 ± 3.79
HTC-1000-HCl	0.383	0.868	3.451	5.52 ± 0.50	0.820 ± 0.009	176 ± 1.96
HC-1200	0.377	0.892	4.637	3.57 ± 0.22	0.756 ± 0.007	134 ± 3.82
HTC-1200	0.377	1.056	5.346	3.82 ± 0.25	0.764 ± 0.017	136 ± 4.17
HTC-1200-HCl	0.385	0.932	3.333	4.09 ± 0.46	0.781 ± 0.012	146 ± 2.59

The lower degree of graphitization of HCl-catalyzed hydrochar-derived carbons was also confirmed by the results obtained from Raman spectroscopy. As can be seen in Table 1, the values of $A_{D1}/(A_G + A_{D1} + A_{D2})$ ratio and FWHM (full width at half maximum) of the D1 peak were higher for HTC-1000-HCl and HTC-1200-HCl in comparison with the other materials carbonized at the same highest temperature. The use of the above-mentioned peak area ratio (instead of the A_{D1}/A_G one) to assess the degree of organization of carbons was proposed by Beyssac et al. as a means to smooth the variability induced by both analytical and fitting procedures [31]. In addition, the FWHM of the D1 peak was proposed by Sadezky et al. as a robust indicator of the structural ordering of carbonaceous materials [25]. Fig. S5 shows a Raman spectrum (as well as the deconvolution and fitting process) for each of the WHH-derived carbons.

Table 2 lists the elemental composition on surface of WHH-derived HCs, which was determined from the acquired survey XPS spectra. Results for WHH-derived pyrolysis char and hydrochar (produced in a pure water medium) are also reported. Only K (the most abundant metallic species in raw biomass, as shown in Table S1) was detected as impurity, with its content significantly higher in non-hydrothermally pretreated HCs. From Table 2 it can also be observed, for all the carbonization temperatures, a clear reduction in the oxygen content (at the expense of an increased carbon content) of the resulting HCs when WHH was hydrothermally pretreated, in spite of the relatively oxygen content on surface measured for the hydrochar (34.0%), which is attributed to the introduction of oxygen-containing functional groups during the course

Table 2
Surface composition (atomic %) obtained via integrated areas of the survey XPS spectra.

Material	C	O	N	K
Pyrolysis char (500 °C)	88.5	10.6	0.92	n.d.
Hydrochar (180 °C, 12 h, in pure water)	65.4	34.0	0.42	0.18
HC-800	89.4	9.53	0.38	0.66
HTC-800	94.4	4.89	0.62	0.06
HTC-800-HCl	96.6	3.17	0.18	0.05
HC-1000	93.0	6.42	0.50	0.11
HTC-1000	95.6	3.72	0.56	0.07
HTC-1000-HCl	97.2	2.67	0.04	0.12
HC-1200	91.2	6.06	0.16	2.59
HTC-1200	96.7	2.76	0.46	0.04
HTC-1200-HCl	97.1	2.51	0.27	0.11

of hydrothermal pretreatment. The decrease in the oxygen content on surface for hydrothermally pretreated HCs, which has also been observed in previous studies [32,33], was further enhanced when HCl was added to the hydrothermal stage.

The high-resolution spectra of C 1s region were deconvoluted into six peaks, corresponding to C—C bonds assigned to aromatic sp^2 carbons (281.7–282.0 eV), C—C bonds assigned to sp^3 carbons and defective carbon structures (282.3–282.9 eV), defective carbons and C—O groups (284.3–285.5 eV), C═O groups (286.9–287.8 eV), O═C—O groups (289.3–290.3 eV), and π—π* transitions (291.7–293.0 eV) [34,35]. For its part, the deconvoluted high-resolution spectra of the O 1s region revealed four peaks consisting of C═O bonds in quinones (528.6–529.6 eV), C—O bonds in hydroxyl and phenolic groups (530.3–530.9 eV), C—O bonds in esters and anhydrides groups plus C═O bonds in carboxylic groups (532.3–533.3 eV), and adsorbed moisture and oxygen (534.1–534.8 eV) [36]. The high-resolution scan of the N 1s region was also deconvoluted into pyridinic N (395.4–396.6 eV), pyrrolic N (397.9–398.7 eV), and quaternary N (400.7–402.5 eV). Results from deconvolution are summarized in Fig. 3 (see also Figs. S6–S8 for deconvoluted high-resolution spectra), from which it can be observed that the percentage of sp^2-bonded carbon atoms (Fig. 3a) increased when the carbonization temperature was higher. However, an increase in the area of peak 3 (mainly assigned to defective carbon structures) also increased with temperature, especially when HCl-assisted hydrothermal pretreatment was performed. This seems to be in clear agreement with the results obtained from Raman spectroscopy and XRD, confirming the relatively poor structural ordering of hydrothermally pretreated carbons, especially for both HC-1000-HCl and HC-1200-HCl materials. Concerning the deconvolution of the O 1s region (see Fig. 3b), it can be deduced that an increase in the carbonization temperature resulted in an increased carbonyl oxygen content and a decreased C—O and carboxylic oxygen contents. It is generally accepted that a higher content of C═O bonds at the expense of C—O ones is positive for reversible adsorption of Na ions on surface, resulting in enhanced slope capacity and ICE values [35,37,38]. Finally, results from deconvolution of the N 1s region (see Fig. 3c) indicate that pyridinic N, and to a lesser extent pyrrolic N, generally disappeared or were converted into quaternary N as carbonization temperature was increased. Nevertheless, the HC-1000-HCl showed the highest pyrrolic N content (and related low quaternary N content), which may also be advantageous for further improving electrochemical performance by facilitating the reversible adsorption-desorption of sodium ions, as reported by Feng et al. [39].

Regarding the textural features, which are summarized in Table 3 (see also Figs. S9 and S10 for adsorption isotherms and pore size distributions, respectively), it should be noted that the HCl-assisted hydrothermal pretreatment resulted in more developed porous carbons compared to the rest of materials carbonized at the same highest temperature. Even at 1200 °C, where the HC-1200 material exhibited very low porosity (due to the enhanced ordering of the graphene-like layers, leading to the shrinkage of micropores [40]), HC-1200-HCl still retained a considerably microporous structure with pore sizes below 0.7 nm (see Fig. S10f). These ultra-micropores can enhance the plateau capacity and improve the ICE by providing fast transport channels for Na ions and simultaneously hinder the contact of the electrolyte with the inner surface [41,42].

Based on the results from physicochemical characterization, one can conclude that the addition of hydrochloric acid during the hydrothermal pretreatment appears as an effective strategy to inhibit an excessive rearrangement of the carbon structure during the course of the high-temperature carbonization step. This can be partially explained by the fact that the oxygen-containing functional groups (OFGs) introduced

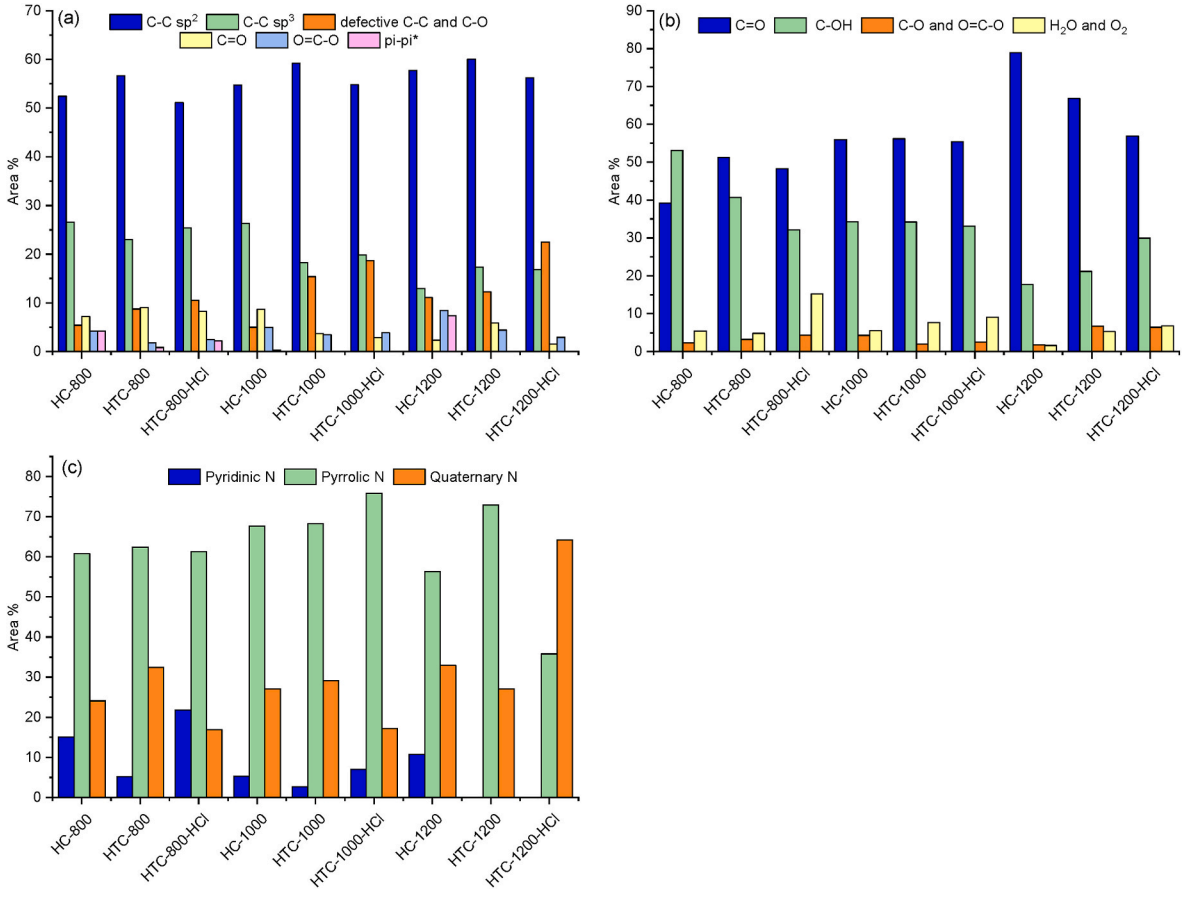

Fig. 3. Contributions (area %) of the different peaks from deconvoluted C 1s (a), O 1s (b), and N 1s (c) binding energy regions.

Table 3
Textural features deduced from the N_2 and CO_2 adsorption isotherms given in Fig. S9.

Material	S_{BET}[a] ($m^2\ g^{-1}$)	S_{BET}[b] ($m^2\ g^{-1}$)	Micropore volume[c] ($cm^3\ g^{-1}$)	Mesopore volume[c] ($cm^3\ g^{-1}$)	Ultramicropore volume[d] ($cm^3\ g^{-1}$)
HC-800	13.63	369.8	0.0114	0.0061	0.1689
HTC-800	61.71	387.9	0.0309	0.0068	0.1799
HTC-800-HCl	461.8	423.1	0.1778	0.0303	0.1959
HC-1000	14.73	417.7	0.0041	0.0110	0.1218
HTC-1000	11.11	401.7	0.0056	0.0108	0.1862
HTC-1000-HCl	95.56	427.6	0.0582	0.0112	0.1994
HC-1200	6.13	114.4	0.0020	0.0065	0.0093
HTC-1200	25.21	208.2	0.0072	0.0243	0.0819
HTC-1200-HCl	103.4	375.3	0.0365	0.0301	0.1797

[a] From N_2 adsorption isotherm at −196 °C.
[b] From CO_2 adsorption isotherm at 0 °C.
[c] From N_2 adsorption data using a NLDFT model.
[d] From CO_2 adsorption data using a NLDFT model.

during HCl-assisted hydrothermal pretreatment can act as inherent activators during thermal annealing, leading to mores structural defects and an increased porosity caused by the decomposition of such OFGs.

3.2. Electrochemical performance of hard carbon-based anodes

The CV curves corresponding to the first three discharge-charge cycles for HC-1000, HTC-1000, and HTC-1000-HCl materials are shown in Fig. 4. The peaks appearing at around 0.01 V (cathodic) and 0.15–0.20 V (anodic) are attributed to the reversible accumulation and release of Na ions in the carbon framework, respectively [43–45]. Concerning the broad cathodic peak appearing only during the first discharge and centered at 0.75–0.85 V, it can be ascribed to the decomposition of the electrolyte and formation of the SEI layer as well as

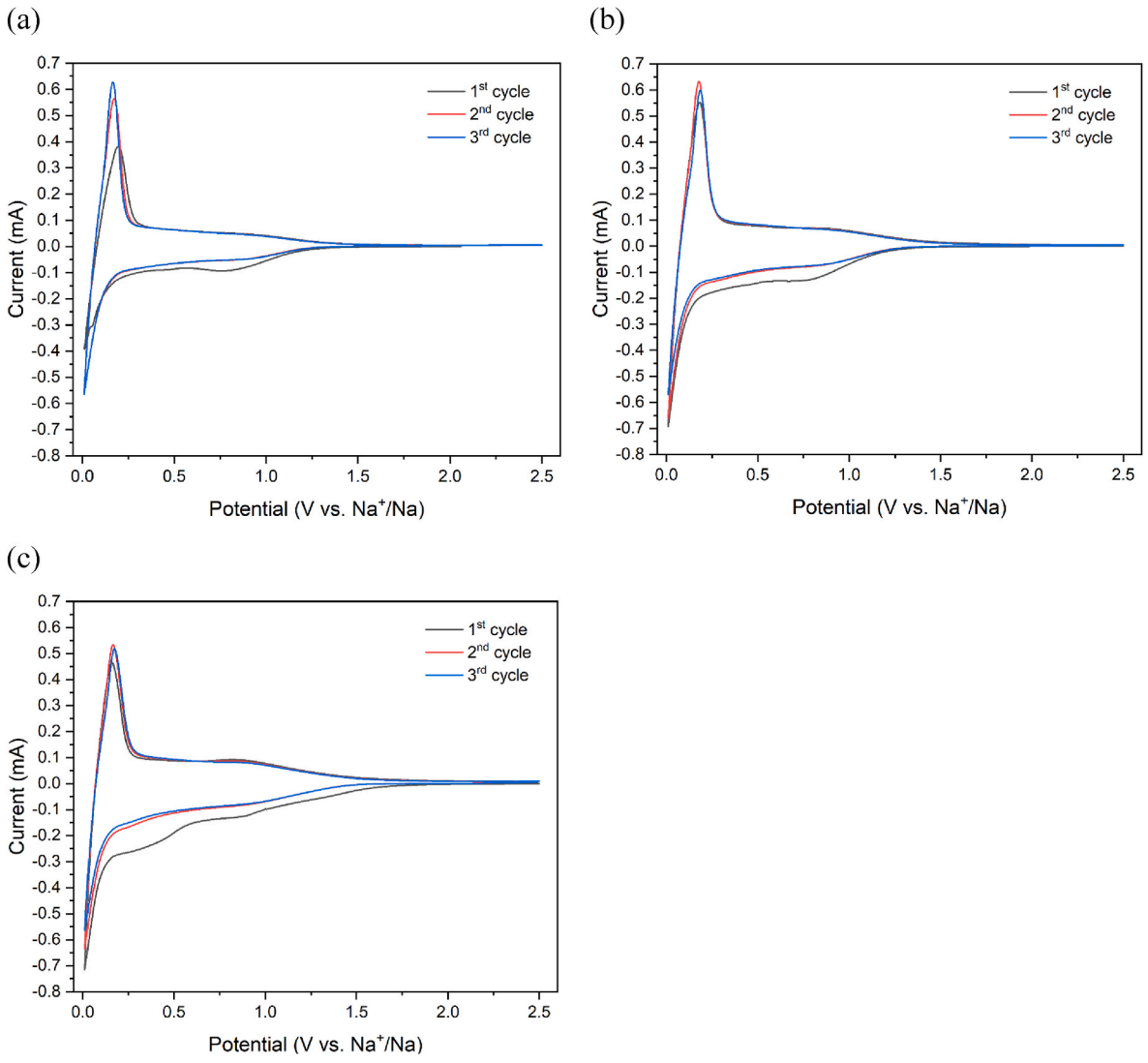

Fig. 4. CV curves of the first three cycles for HC-1000 (a), HTC-1000 (b); and HTC-1000-HCl (c).

the irreversible trapping of Na ions in structural defects and surface functional groups. In the case of the HTC-1000-HCl-based electrode, an additional peak centered at 0.3–0.4 V was also observed during the first discharge. This fact could be explained by the higher specific surface area and micropore volume of HTC-1000-HCl, which can enhance contact between the electrolyte and the inner surface of the electrode, resulting in a slightly thicker SEI and lower ICE.

Fig. 5 shows the first five GCD cycles (at a current density of 0.03 A g^{-1}) for selected WH-derived HCs using two-electrode cells. As can clearly be seen in Fig. 5f, an increase in the carbonization temperature

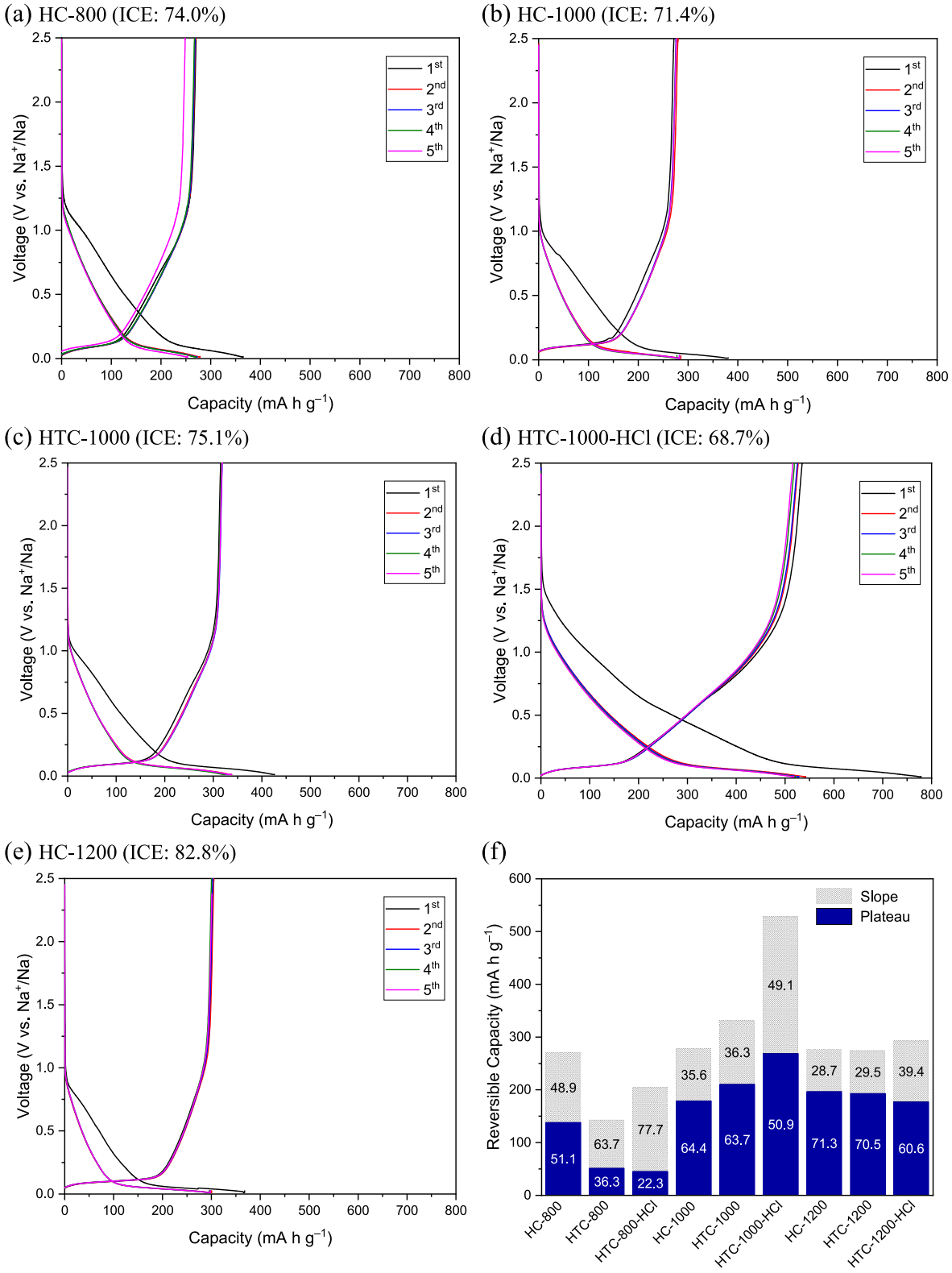

Fig. 5. GCD profiles (using two-electrode cells at 0.03 A g^{-1}) for the first five cycles of HC-800 (a), HC-1000 (b), HTC-1000 (c), HTC-1000-HCl (d), and HC-1200 (e). Plateau and slope contributions (percentage) during reversible sodiation (f).

for non-hydrothermally pretreated HCs was translated into a higher contribution from the plateau region at the expense of that from the slope one with no significant changes in the total reversible capacity (ca. 270 mA h g^{-1}). This was consistent with the lower content of heteroatom-containing functional groups on surface and higher degree of graphitization observed for said HCs as the highest treatment temperature increased.

The effect on hydrothermal pretreatment on GCD profiles, however, was clearly dependent on both the carbonization temperature and hydrothermal medium. For instance, hydrothermally treated HCs carbonized at 800 °C exhibited a poorer electrochemical performance compared to HC-800, showing a very low contribution from the plateau. This was due to the low ICE values observed for both HTC-800 and HTC-800-HCl active materials (48% and 39%, respectively), as shown in Fig. S11. The pronounced irreversible first sodiation is likely ascribed to an excessive content of structural defects, which can hinder the mobility of Na ions by trapping a fraction of them and generating a repulsive electric field [46].

The above-mentioned trend changed radically for HCs produced at 1000 °C. In this case, the hydrothermally pretreatment, especially when it was conducted using an acidic medium, resulted in an improvement of the reversible specific capacity. The HTC-1000-HCl exhibited an impressive value of 535 mA h g^{-1} with almost equal contributions from the slope and plateau regions. This excellent capacity could be attributed to a combination of features that synergistically contribute to the overall outcome: (*i*) an appropriate number of defects for reversible adsorption of Na ions, leading to a large slope capacity and an acceptable ICE of 69%; (*ii*) an improved graphitization degree (compared with HCs carbonized at 800 °C) with appropriate interlayer spacing; and (*iii*) a number of closed nanovoids (due to the folding of curved carbon layers, as shown in Fig. 2f), which can accommodate the deposited quasi-metallic Na in the plateau region [38,47,48].

For the HCs carbonized at the highest temperature (1200 °C), an unequivocally greater contribution to the reversible capacity of the plateau region was observed compared to that of the slope region (see Fig. 5f). This can be attributed to the increased ordering of the carbon structure, resulting in a lower number of defects on one hand, and the elongation of graphene-like carbon layers (particularly evident in both HC-1200 and HTC-1200 in light of the L_a values listed in Table 1), promoting the formation of closed-pore microstructures on the other hand. It is worth noting the excellent ICE measured for HC-1200 (83%). However, both HTC-1200 and HTC-1200-HCl exhibited substantially reduced ICE values of 58% and 65%, respectively (see Fig. S11). This can be attributed, at least in part, to the fact that the hydrothermally pretreated HCs exhibited a more hierarchical pore size distribution, featuring comparatively larger volumes of both micropores and mesopores, in contrast to the pore structure of the HC-800 carbon (see Table 3). Thus, decomposition of the electrolyte on the surface of reachable open pores (large micropores and mesopores) and subsequent SEI formation can result in more irreversible consumption of Na-ions

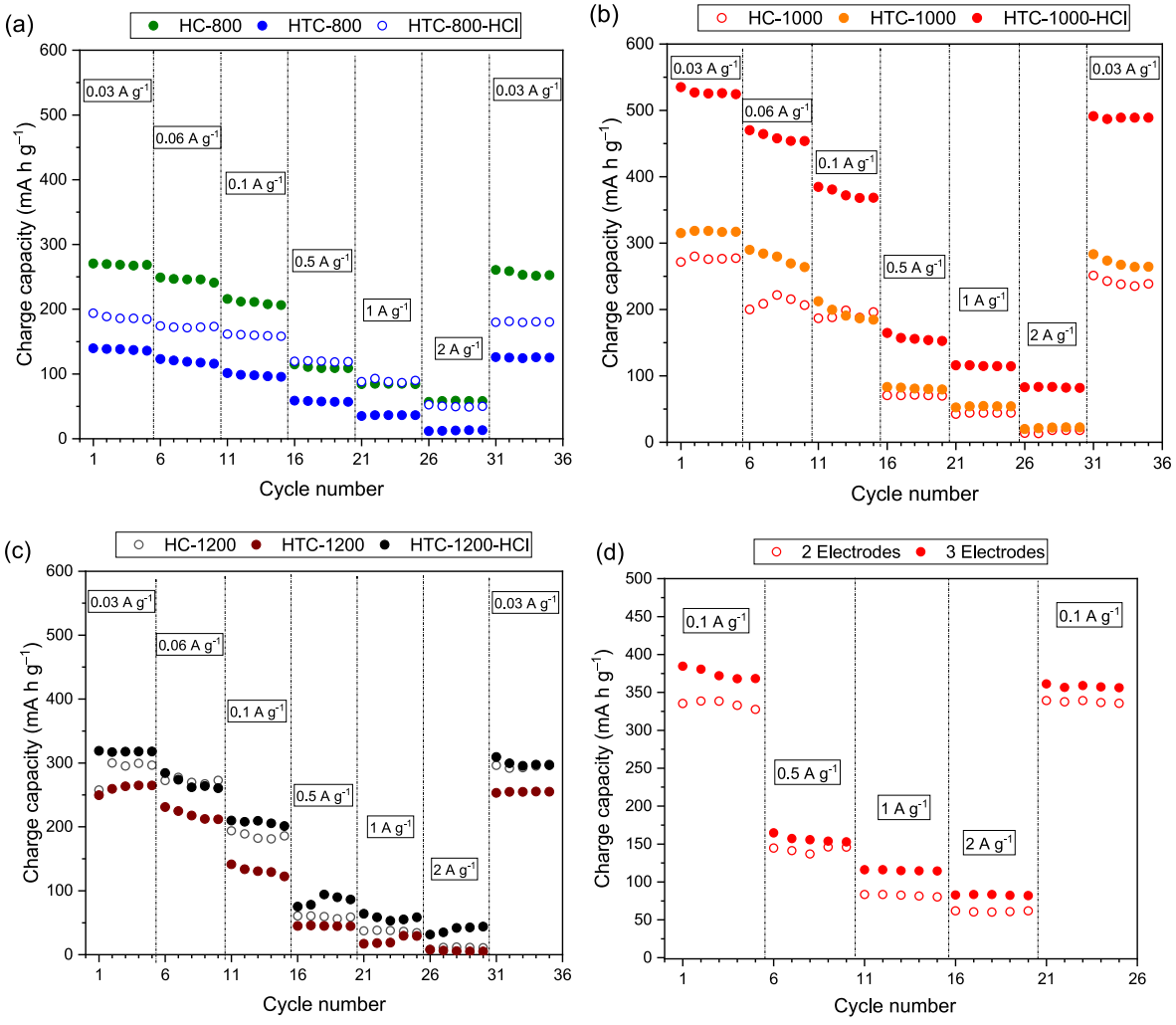

Fig. 6. Charge specific capacities at various current densities ranging from 0.03 to 2 A g^{-1} (two-electrode cell setup) of WHH-derived HCs carbonized at 800 °C (a), 1000 °C (b) and 1200 °C (c). Plot (d) compares the charge capacity of HTC-1000-HCl measured using 2-electrode and 3-electrode cells.

when HTC-1200 and HTC-1200-HCl were used as working electrodes.

With regard to the rate capability of the HC-based anodes (assessed through additional GCD cycles at increasing current densities) Fig. 6 clearly shows that HTC-1000-HCl outperformed all other materials in all cases, showing reversible charge capacities of 458, 372, 156, 115 and 83 mA h g^{-1} when cycled at 0.06, 0.1, 0.5, 1, and 2 A g^{-1}, respectively (see Tables S2 and S3 for detailed charge capacity values). Interestingly, comparable charge capacities were recorded upon completion of the rate capability tests and subsequent cycling of the electrodes at 0.03 A g^{-1} (ca. 95% of capacity retention for HTC-1000-HCl), thus demonstrating the stability of all WHH-derived hard carbons at high current rates.

In order to compare the electrochemical performance of the HCs reported herein (in particular HTC-1000-HCl), Table 4 summarizes the outcomes reported in the literature for plant-derived HCs produced via hydrothermal pretreatment and subsequent carbonization. After comparing the data given in the table, it can be concluded that the performance of the HTC-1000-HCl material is excellent, particularly in terms of reversible specific capacity at low and moderate current density (i.e., up to 0.1 A g^{-1}). In addition, the ICE measured for this hard carbon (69%) can be considered as appropriate in light of the relatively moderate carbonization temperature (1000 °C). Higher ICE values were attained when carbonization temperature was set to 1200 °C (e.g., 83% for the HC-1200 material reported in this study and 78% reported by Nieto et al. for a sunflower seed-derived HC [18]), 1300 °C (e.g., 77% for a reed straw-derived HC [49]), and 1400 °C (e.g., 80% for an alder driftwood-derived HC [50]). Nevertheless, as shown in Fig. 6c, HC-1200 showed a notably lower rate capability compared to HTC-1000-HCl, probably as a consequence of its low open porosity and the associated high diffusion resistance.

Fig. 6d compares the results from the rate capability tests conducted for the best-performing material (HTC-1000-HCl) using two- and three-electrode half-cells. As expected, an underestimation of the specific capacity (which ranged from 9% to 28%) was confirmed when employing two-electrode half-cells. This phenomenon could be ascribed to the development of a passivation layer on the surface of the metallic sodium counter electrode during discharge [16,26,51].

To gain more insights into the kinetics and mechanism underlaying sodiation and desodiation processes, Fig. 7 shows plots of the apparent diffusion coefficients (D_{Na}^{+}), which were calculated from GITT measurements (see supplementary data for further details and Tables S4–S6 for $D_{Na}{}^{+}$ values). As expected, a decrease in ion diffusivity was observed when the voltage decreased from sloping to plateau region during discharge. Nevertheless, this decrease was much more attenuated for HTC-1000 and HTC-1000-HCl materials. This could be associated to the larger volume of ultramicropores of these hydrothermally pretreated HCs (see Table 3), which could lead to a faster diffusion of Na ions from the surface to the locally-ordered graphene stacks and closed pores for intercalation and pore filling, respectively. The increase in diffusivity observed at the end of the plateau region (ca. 0.04 V) could be ascribed to sodium plating in the pores of the carbon structure, as reported by Ledwoch et al. [58]. The reversibility of the process was confirmed by observing that the change in diffusivity during charging (as plotted in Fig. 7b) was comparable to that measured during sodiation.

To check the cycling stability of HTC-1000-HCl, 300 discharge-charge cycles were performed at 1 A g^{-1} (following an initial set of five cycles at 0.1 A g^{-1}) using a three-electrode cell. Fig. 8 displays the evolution of the measured charge specific capacity over the cycles. Throughout the initial 20 cycles, there was a marginal increase in capacity, rising from 185 to 201 mA h g^{-1}, probably as a result of the fact that small mesopores and large micropores are becoming more accessible to the electrolyte over time, thereby creating additional active sites [59]. Subsequently, a pronounced decline in capacity was noted, persisting until the 140th cycle, after which the trend shifted to a more gradual decrease. The observed poor stability at a relatively high current rate (62% of capacity retention) can be attributed to parasitic reactions at the relatively thick and nonuniform carbonates-based SEI [60]. However, when the current rate was restored to its initial value (0.1 A g^{-1}), a satisfactory 91% of capacity retention (with respect to the values measured throughout the first five cycles at the same current rate) was measured.

In contrast to carbonate-based electrolytes, ether-based ones are known for forming a thin and inorganic-rich SEI film, which can enhance ICE and cycling stability [61,62]. Fig. 8 also plots the results from the stability test when $NaPF_6$ in diglyme (1 mol dm^{-3}) was used as electrolyte. Clearly, the cycling stability of the working electrode significantly improved, with an 85% of capacity retention after 300 cycles at 1 A g^{-1}. Furthermore, the ICE increased from 69% to 78% (see Fig. S12). The lower initial capacity observed for the $NaPF_6$-diglyme, compared with that of NaTFSI-EC/DMC, was also reported in an earlier study [63]. A possible explanation for this could be the fact that intercalation of diglyme-Na^{+} complexes [64], which has been evidenced in graphite, could be hindered in hard carbons, where the highly cross-linked structure cannot withstand the strain induced by the large volume expansion.

4. Conclusions

WHH-derived hard carbons produced via hydrothermal pretreatment and subsequent carbonization have been proven to be low-cost and sustainable alternatives to be used as negative electrodes in SIBs. Among all the materials tested, the one hydrothermally processed in 2 mol dm^{-3} HCl solution and carbonized at 1000 °C clearly showed the best electrochemical performance. This material exhibited a set of features that

Table 4
Electrochemical performance as anodes in SIBs of plant-derived HCs produced via hydrothermal pretreatment and subsequent carbonization.

Biomass Precursor	Hydrothermal pretreatment	Carbonization temperature	Reversible capacity (mA h g^{-1}) at current density (A g^{-1})	ICE (%)	Ref.
Holly leaf	In water at 180 °C during 10 h	800 °C	318 at 0.02; 127 at 0.2	50	[52]
Ginkgo leaf	In H_2SO_4 (2 mol dm^{-3}) at 250 °C during 12 h	700 °C (with KOH activation)	200 at 0.2	31	[53]
Reed straw	In water at 200 °C during 24 h	1300 °C	372 at 0.025; 284 at 0.1	77	[49]
Pistachio shells	In NaOH (3 mol dm^{-3}) at 165 °C during 6 h	1000 °C	320 at 0.03; 171 at 0.3; 95 at 1.2	62	[54]
Rambutan peel	In NaOH (1 mol dm^{-3}) at 200 °C during 20 h	1000 °C	240 at 0.03; 172 at 0.3, 155 at 0.6	55	[55]
Litchi pericarp	In diluted H_2SO_4 at 180 °C during 24 h	1200 °C	317 at 0.02; 271 at 0.1; 182 at 0.5; 109 at 1; 76 at 2	70	[56]
Lotus leaves	In HCl (1 mol dm^{-3}) at 180 °C during 10 h	800 °C	273 at 0.02; 110 at 0.8; 78 at 2	66	[32]
Corn stalk	In water at 160 °C during 12 h	1000 °C	270 at 0.06; 238 at 0.6; 215 at 1.5; 172 at 3	64	[57]
Sunflower seed	In water at 250 °C during 24 h	1200 °C	280 at 0.025; 170 at 0.37 (120 after 1000 cycles)	76	[18]
Alder driftwood	In water at 220 °C during 6 h	1400 °C	305 at 0.037; 285 at 0.37	80	[50]
Waste hemp hurd	In HCl (2 mol dm^{-3}) at 180 °C during 12 h	1000 °C	535 at 0.03; 458 at 0.06; 372 at 0.1; 156 at 0.5; 115 at 1; 83 at 2	69	This study

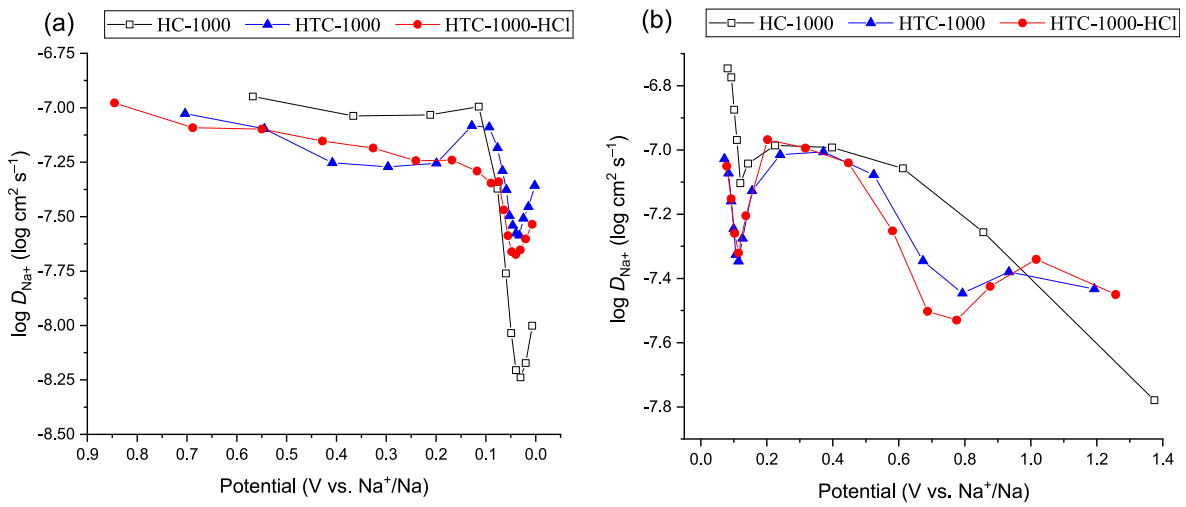

Fig. 7. D^+_{Na} values calculated from GITT measurements along sodiation (discharge) (a) and desodiation (charge) (b) of WHH-derived carbons produced at 1000 °C.

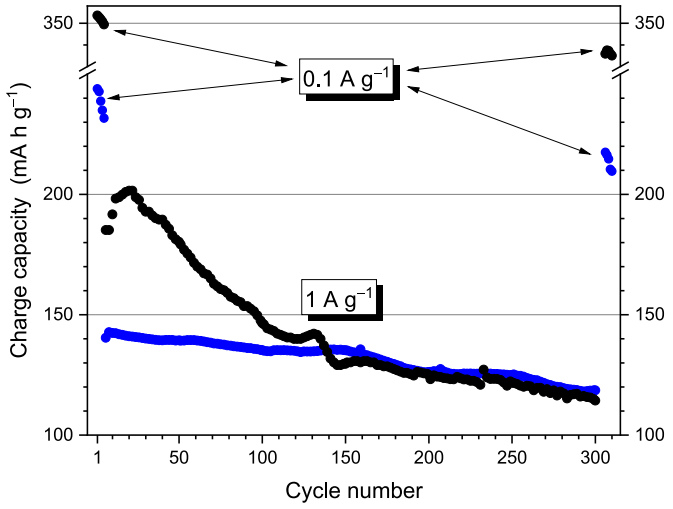

Fig. 8. Cycling performance of the HTC-1000-HCl-based electrode at 1 A g^{-1} using NaTFSI in EC/DMC (black circles) and $NaPF_6$ in diglyme (blue circles) as electrolyte. (For interpretation of the references to colour in this figure legend, the reader is referred to the Web version of this article.)

contribute to an excellent balance between slope and plateau capacities, resulting in outstanding Na ion storage capacity at low current rates and more than acceptable rate capabilities (i.e., 535, 372, and 115 mA h g^{-1} when cycled at 0.03, 0.1, and 1 A g^{-1}, respectively). Noteworthy among these features are the relatively large number of defects, the interconnected pore network (mostly ultramicroporous), appropriate interlayer spacing, and the presence of closed nanovoids in its structure. Regarding cycling stability, the active material exhibited a much better performance when the initial electrolyte (NaTFSI in EC/DMC 1 mol dm^{-3}) was replaced by an ether-based one ($NaPF_6$ in diglyme 1 mol dm^{-3}). However, this improvement in stability was at the expense of a certain loss of specific capacity. Further research is needed to further clarify the role of the electrolyte formulation and test the best-performing hard carbon in full-cell setups.

CRediT authorship contribution statement

Daniel Antorán: Writing – original draft, Methodology, Investigation, Conceptualization. **Darío Alvira:** Methodology, Conceptualization. **Víctor Sebastián:** Resources, Investigation. **Joan J. Manyà:** Writing – review & editing, Supervision, Funding acquisition, Conceptualization.

Data availability

Data will be made available on request.

Acknowledgments

This work is part of the research project PID2019-107737RB-I00, funded by MCIN/AEI/10.13039/501100011033 and "ERDF A way of making Europe". The authors acknowledge the funding from the Aragon Government (Ref. T22_23R). Darío Alvira also acknowledges the funding from the Aragon Government with a grant for postgraduate research contracts (2019–2023). LMA-ELECMI and NANBIOSIS ICTs are gratefully acknowledged.

Appendix A. Supplementary data

Supplementary data to this article can be found online at https://doi.org/10.1016/j.biombioe.2024.107197.

References

[1] M. Fichtner, K. Edström, E. Ayerbe, M. Berecibar, A. Bhowmik, I.E. Castelli, S. Clark, R. Dominko, M. Erakca, A.A. Franco, A. Grimaud, B. Horstmann, A. Latz, H. Lorrmann, M. Meeus, R. Narayan, F. Pammer, J. Ruhland, H. Stein, T. Vegge, M. Weil, Rechargeable batteries of the future—the state of the art from a BATTERY 2030+ perspective, Adv. Energy Mater. 12 (2022) 2102904, https://doi.org/10.1002/AENM.202102904.

[2] P.K. Nayak, L. Yang, W. Brehm, P. Adelhelm, From lithium-ion to sodium-ion batteries: advantages, challenges, and surprises, Angew. Chem. Int. Ed. 57 (2018) 102–120, https://doi.org/10.1002/anie.201703772.

[3] Z.L. Xu, G. Yoon, K.Y. Park, H. Park, O. Tamwattana, S. Joo Kim, W.M. Seong, K. Kang, Tailoring sodium intercalation in graphite for high energy and power sodium ion batteries, Nat. Commun. 10 (2019) 2598, https://doi.org/10.1038/s41467-019-10551-z.

[4] H. Kim, J. Hong, Y.U. Park, J. Kim, I. Hwang, K. Kang, Sodium storage behavior in natural graphite using ether-based electrolyte systems, Adv. Funct. Mater. 25 (2015) 534–541, https://doi.org/10.1002/adfm.201402984.

[5] Q. Liu, R. Xu, D. Mu, G. Tan, H. Gao, N. Li, R. Chen, F. Wu, Progress in electrolyte and interface of hard carbon and graphite anode for sodium-ion battery, Carbon Energy 4 (2022) 458–479, https://doi.org/10.1002/CEY2.120.

[6] C. Nita, B. Zhang, J. Dentzer, C. Matei Ghimbeu, Hard carbon derived from coconut shells, walnut shells, and corn silk biomass waste exhibiting high capacity for Na-ion batteries, J. Energy Chem. 58 (2021) 207–218, https://doi.org/10.1016/j.jechem.2020.08.065.

[7] D. Alvira, D. Antorán, J.J. Manyà, Plant-derived hard carbon as anode for sodium-ion batteries: a comprehensive review to guide interdisciplinary research, Chem. Eng. J. 447 (2022) 137468, https://doi.org/10.1016/j.cej.2022.137468.

[8] N. Sun, J. Qiu, B. Xu, Understanding of sodium storage mechanism in hard carbons: ongoing development under debate, Adv. Energy Mater. 12 (2022) 2200715, https://doi.org/10.1002/AENM.202200715.

[9] Y. Zhu, M. Chen, Q. Li, C. Yuan, C. Wang, A porous biomass-derived anode for high-performance sodium-ion batteries, Carbon 129 (2018) 695–701, https://doi.org/10.1016/j.carbon.2017.12.103.
[10] Y. Li, S. Xu, X. Wu, J. Yu, Y. Wang, Y.S. Hu, H. Li, L. Chen, X. Huang, Amorphous monodispersed hard carbon micro-spherules derived from biomass as a high performance negative electrode material for sodium-ion batteries, J. Mater. Chem. A 3 (2015) 71–77, https://doi.org/10.1039/c4ta05451b.
[11] Y. Li, Y.S. Hu, H. Li, L. Chen, X. Huang, A superior low-cost amorphous carbon anode made from pitch and lignin for sodium-ion batteries, J. Mater. Chem. A 4 (2015) 96–104, https://doi.org/10.1039/c5ta08601a.
[12] Z.L. Yu, S. Xin, Y. You, L. Yu, Y. Lin, D.W. Xu, C. Qiao, Z.H. Huang, N. Yang, S. H. Yu, J.B. Goodenough, Ion-catalyzed synthesis of microporous hard carbon embedded with expanded nanographite for enhanced lithium/sodium storage, J. Am. Chem. Soc. 138 (2016) 14915–14922, https://doi.org/10.1021/jacs.6b06673.
[13] European Commission, Hemp production in the EU. https://agriculture.ec.europa.eu/farming/crop-productions-and-plant-based-products/hemp_en#hempproductionintheeu. (Accessed 27 January 2023).
[14] S. Matassa, G. Esposito, F. Pirozzi, S. Papirio, Exploring the biomethane potential of different industrial hemp (Cannabis sativa L.) biomass residues, Energies 13 (2020) 3361, https://doi.org/10.3390/en13133361.
[15] W. Sun, S.M. Lipka, C. Swartz, D. Williams, F. Yang, Hemp-derived activated carbons for supercapacitors, Carbon 103 (2016) 181–192, https://doi.org/10.1016/j.carbon.2016.02.090.
[16] D. Antorán, D. Alvira, M.E. Peker, H. Malón, S. Irusta, V. Sebastián, J.J. Manyà, Waste hemp hurd as a sustainable precursor for affordable and high-rate hard carbon-based anodes in sodium-ion batteries, Energy Fuels 37 (2023) 9650–9661, https://doi.org/10.1021/acs.energyfuels.3c01040.
[17] Z. Xu, J. Wang, Z. Guo, F. Xie, H. Liu, H. Yadegari, M. Tebyetekerwa, M.P. Ryan, Y. S. Hu, M.M. Titirici, The role of hydrothermal carbonization in sustainable sodium-ion battery anodes, Adv. Energy Mater. 12 (2022) 2200208, https://doi.org/10.1002/AENM.202200208.
[18] N. Nieto, J. Porte, D. Saurel, L. Djuandhi, N. Sharma, A. Lopez-Urionabarrenechea, V. Palomares, T. Rojo, Use of hydrothermal carbonization to improve the performance of biowaste-derived hard carbons in sodium ion-batteries, ChemSusChem 16 (2023) e202301053, https://doi.org/10.1002/cssc.202301053.
[19] O.S. Djandja, R.K. Liew, C. Liu, J. Liang, H. Yuan, W. He, Y. Feng, B.G. Lougou, P. G. Duan, X. Lu, S. Kang, Catalytic hydrothermal carbonization of wet organic solid waste: a review, Sci. Total Environ. 873 (2023) 162119, https://doi.org/10.1016/J.SCITOTENV.2023.162119.
[20] S. Zhang, K. Sheng, W. Yan, J. Liu, E. Shuang, M. Yang, X. Zhang, Bamboo derived hydrochar microspheres fabricated by acid-assisted hydrothermal carbonization, Chemosphere 263 (2021) 128093, https://doi.org/10.1016/J.CHEMOSPHERE.2020.128093.
[21] L. Fan, Z. Shi, Q. Ren, L. Yan, F. Zhang, L. Fan, Nitrogen-doped lignin based carbon microspheres as anode material for high performance sodium ion batteries, Green Energy Environ. 6 (2021) 220–228, https://doi.org/10.1016/j.gee.2020.06.005.
[22] G. Greco, M. Videgain, C. Di Stasi, B. González, J.J. Manyà, Evolution of the mass-loss rate during atmospheric and pressurized slow pyrolysis of wheat straw in a bench-scale reactor, J. Anal. Appl. Pyrolysis 136 (2018) 18–26, https://doi.org/10.1016/j.jaap.2018.11.007.
[23] G. Greco, C. Di Stasi, F. Rego, B. González, J.J. Manyà, Effects of slow-pyrolysis conditions on the products yields and properties and on exergy efficiency: a comprehensive assessment for wheat straw, Appl. Energy 279 (2020) 115842, https://doi.org/10.1016/j.apenergy.2020.115842.
[24] D. Alvira, D. Antorán, J.J.J.J. Manyà, Assembly and electrochemical testing of renewable carbon-based anodes in SIBs: a practical guide, J. Energy Chem. 75 (2022) 457–477, https://doi.org/10.1016/j.jechem.2022.09.002.
[25] A. Sadezky, H. Muckenhuber, H. Grothe, R. Niessner, U. Pöschl, Raman microspectroscopy of soot and related carbonaceous materials: spectral analysis and structural information, Carbon 43 (2005) 1731–1742, https://doi.org/10.1016/j.carbon.2005.02.018.
[26] D. Alvira, D. Antorán, M. Vidal, V. Sebastian, J.J. Manyà, Vine shoots-derived hard carbons as anodes for sodium-ion batteries: role of annealing temperature in regulating their structure and morphology, Batter. Supercaps 6 (2023), https://doi.org/10.1002/batt.202300233.
[27] Y. Xi, Y. Wang, D. Yang, Z. zhang, W. Liu, Q. Li, X. Qiu, K2CO3 activation enhancing the graphitization of porous lignin carbon derived from enzymatic hydrolysis lignin for high performance lithium-ion storage, J. Alloys Compd. 785 (2019) 706–714, https://doi.org/10.1016/j.jallcom.2019.01.039.
[28] K.G. Raj, P.A. Joy, Role of localized graphitization on the electrical and magnetic properties of activated carbon, J. Am. Ceram. Soc. 100 (2017) 5151–5161, https://doi.org/10.1111/JACE.15035.
[29] S. Komaba, W. Murata, T. Ishikawa, N. Yabuuchi, T. Ozeki, T. Nakayama, A. Ogata, K. Gotoh, K. Fujiwara, Electrochemical Na insertion and solid electrolyte interphase for hard-carbon electrodes and application to Na-ion batteries, Adv. Funct. Mater. 21 (2011) 3859–3867, https://doi.org/10.1002/ADFM.201100854.
[30] X. Dou, I. Hasa, D. Saurel, C. Vaalma, L. Wu, D. Buchholz, D. Bresser, S. Komaba, S. Passerini, Hard carbons for sodium-ion batteries: structure, analysis, sustainability, and electrochemistry, Mater. Today 23 (2019) 87–104, https://doi.org/10.1016/j.mattod.2018.12.040.
[31] O. Beyssac, B. Goffé, J.P. Petitet, E. Froigneux, M. Moreau, J.N. Rouzaud, On the characterization of disordered and heterogeneous carbonaceous materials by Raman spectroscopy, Spectrochim. Acta Part A Mol. Biomol. Spectrosc. 59 (2003) 2267–2276, https://doi.org/10.1016/S1386-1425(03)00070-2.
[32] C.C. Wang, W.L. Su, Understanding acid pretreatment of lotus leaves to prepare hard carbons as anodes for sodium ion batteries, Surf. Coating. Technol. 415 (2021) 127125, https://doi.org/10.1016/j.surfcoat.2021.127125.
[33] C. Li, D. He, Z.-H. Huang, M.-X. Wang, Hierarchical micro-/mesoporous carbon derived from rice husk by hydrothermal pre-treatment for high performance supercapacitor, J. Electrochem. Soc. 165 (2018) A3334–A3341, https://doi.org/10.1149/2.0121814JES/XML.
[34] M. Smith, L. Scudiero, J. Espinal, J.S. McEwen, M. Garcia-Perez, Improving the deconvolution and interpretation of XPS spectra from chars by ab initio calculations, Carbon 110 (2016) 155–171, https://doi.org/10.1016/J.CARBON.2016.09.012.
[35] C. Chen, Y. Huang, Y. Zhu, Z. Zhang, Z. Guang, Z. Meng, P. Liu, Nonignorable influence of oxygen in hard carbon for sodium ion storage, ACS Sustain. Chem. Eng. 8 (2020) 1497–1506, https://doi.org/10.1021/acssuschemeng.9b05948.
[36] J.H. Zhou, Z.J. Sui, J. Zhu, P. Li, D. Chen, Y.C. Dai, W.K. Yuan, Characterization of surface oxygen complexes on carbon nanofibers by TPD, XPS and FT-IR, Carbon 45 (2007) 785–796, https://doi.org/10.1016/J.CARBON.2006.11.019.
[37] H. Zhao, J. Ye, W. Song, D. Zhao, M. Kang, H. Shen, Z. Li, Insights into the surface oxygen functional group-driven fast and stable sodium adsorption on carbon, ACS Appl. Mater. Interfaces 12 (2020) 6991–7000, https://doi.org/10.1021/ACSAMI.9B11627/ASSET/IMAGES/LARGE/AM9B11627_0005.JPEG.
[38] T. Xu, X. Qiu, X. Zhang, Y. Xia, Regulation of surface oxygen functional groups and pore structure of bamboo-derived hard carbon for enhanced sodium storage performance, Chem. Eng. J. 452 (2023) 139514, https://doi.org/10.1016/J.CEJ.2022.139514.
[39] X. Feng, Y. Bai, L. Zheng, M. Liu, Y. Li, R. Zhao, Y. Li, C. Wu, Effect of different nitrogen configurations on sodium storage properties of carbon anodes for sodium ion batteries, ACS Appl. Mater. Interfaces 13 (2021) 56285–56295, https://doi.org/10.1021/ACSAMI.1C18464.
[40] K. Kim, D.G. Lim, C.W. Han, S. Osswald, V. Ortalan, J.P. Youngblood, V.G. Pol, Tailored carbon anodes derived from biomass for sodium-ion storage, ACS Sustain. Chem. Eng. 5 (2017) 8720–8728, https://doi.org/10.1021/acssuschemeng.7b01497.
[41] Q. Meng, Y. Lu, F. Ding, Q. Zhang, L. Chen, Y.S. Hu, Tuning the closed pore structure of hard carbons with the highest Na storage capacity, ACS Energy Lett. 4 (2019) 2608–2612, https://doi.org/10.1021/ACSENERGYLETT.9B01900.
[42] Z. Zheng, S. Hu, W. Yin, J. Peng, R. Wang, J. Jin, B. He, Y. Gong, H. Wang, H.J. Fan, CO2-Etching creates abundant closed pores in hard carbon for high-plateau-capacity sodium storage, Adv. Energy Mater. (2023) 2303064, https://doi.org/10.1002/AENM.202303064.
[43] L. Xiao, Y. Cao, W.A. Henderson, M.L. Sushko, Y. Shao, J. Xiao, W. Wang, M. H. Engelhard, Z. Nie, J. Liu, Hard carbon nanoparticles as high-capacity, high-stability anodic materials for Na-ion batteries, Nano Energy 19 (2016) 279–288, https://doi.org/10.1016/J.NANOEN.2015.10.034.
[44] E.M. Lotfabad, J. Ding, K. Cui, A. Kohandehghan, W.P. Kalisvaart, M. Hazelton, D. Mitlin, High-density sodium and lithium ion battery anodes from banana peels, ACS Nano 8 (2014) 7115–7129, https://doi.org/10.1021/nn502045y.
[45] T. Zhang, J. Mao, X. Liu, M. Xuan, K. Bi, X.L. Zhang, J. Hu, J. Fan, S. Chen, G. Shao, Pinecone biomass-derived hard carbon anodes for high-performance sodium-ion batteries, RSC Adv. 7 (2017) 41504–41511, https://doi.org/10.1039/c7ra07231g.
[46] L. Xiao, H. Lu, Y. Fang, M.L. Sushko, Y. Cao, X. Ai, H. Yang, J. Liu, Low-defect and low-porosity hard carbon with high coulombic efficiency and high capacity for practical sodium ion battery anode, Adv. Energy Mater. 8 (2018) 1703238, https://doi.org/10.1002/aenm.201703238.
[47] Y. Li, Y. Lu, Q. Meng, A.C.S. Jensen, Q. Zhang, Q. Zhang, Y. Tong, Y. Qi, L. Gu, M. M. Titirici, Y.S. Hu, Regulating pore structure of hierarchical porous waste cork-derived hard carbon anode for enhanced Na storage performance, Adv. Energy Mater. 9 (2019) 1902852, https://doi.org/10.1002/AENM.201902852.
[48] S. Zhou, Z. Tang, Z. Pan, Y. Huang, L. Zhao, X. Zhang, D. Sun, Y. Tang, A. S. Dhmees, H. Wang, Regulating closed pore structure enables significantly improved sodium storage for hard carbon pyrolyzing at relatively low temperature, SusMat 2 (2022) 357–367, https://doi.org/10.1002/SUS2.60.
[49] J. Wang, L. Yan, Q. Ren, L. Fan, F. Zhang, Z. Shi, Facile hydrothermal treatment route of reed straw-derived hard carbon for high performance sodium ion battery, Electrochim. Acta 291 (2018) 188–196, https://doi.org/10.1016/j.electacta.2018.08.136.
[50] A.F. Qatarneh, C. Dupont, J. Michel, L. Simonin, A. Beda, C. Matei Ghimbeu, V. Ruiz-Villanueva, D. da Silva, H. Piégay, M.J. Franca, River driftwood pretreated via hydrothermal carbonization as a sustainable source of hard carbon for Na-ion battery anodes, J. Environ. Chem. Eng. 9 (2021) 106604, https://doi.org/10.1016/J.JECE.2021.106604.
[51] J. Conder, C. Vaulot, C. Marino, C. Villevieille, C.M. Ghimbeu, Chitin and chitosan - structurally related precursors of dissimilar hard carbons for Na-ion battery, ACS Appl. Energy Mater. 2 (2019) 4841–4852, https://doi.org/10.1021/acsaem.9b00545.
[52] P. Zheng, T. Liu, X. Yuan, L. Zhang, Y. Liu, J. Huang, S. Guo, Enhanced performance by enlarged nano-pores of holly leaf-derived lamellar carbon for sodium-ion battery anode, Sci. Rep. 6 (2016) 1–9, https://doi.org/10.1038/srep26246.
[53] E. Hao, W. Liu, S. Liu, Y. Zhang, H. Wang, S. Chen, F. Cheng, S. Zhao, H. Yang, Rich sulfur doped porous carbon materials derived from ginkgo leaves for multiple electrochemical energy storage devices, J. Mater. Chem. A 5 (2017) 2204–2214, https://doi.org/10.1039/C6TA08169J.
[54] S.-D. Xu, Y. Zhao, S. Liu, X. Ren, L. Chen, W. Shi, X. Wang, D. Zhang, Curly hard carbon derived from pistachio shells as high-performance anode materials for

sodium-ion batteries, J. Mater. Sci. 53 (2018) 12334–12351, https://doi.org/10.1007/s10853-018-2472-4.
[55] A.A. Arie, H. Kristianto, H. Muljana, L. Stievano, Rambutan peel based hard carbons as anode materials for sodium ion battery, Fullerenes Nanotub, Carbon Nanostructures 27 (2019) 953–960, https://doi.org/10.1080/1536383X.2019.1671372.
[56] Z. Zhu, X. Zeng, H. Wu, Y. Wang, H. Cheng, P. Dong, X. Li, Y. Zhang, H. Liu, Green energy application technology of litchi pericarp-derived carbon material with high performance, J. Clean. Prod. 286 (2021) 124960, https://doi.org/10.1016/j.jclepro.2020.124960.
[57] L. Cong, G. Tian, D. Luo, X. Ren, X. Xiang, Hydrothermally assisted transformation of corn stalk wastes into high-performance hard carbon anode for sodium-ion batteries, J. Electroanal. Chem. 871 (2020) 114249, https://doi.org/10.1016/J.JELECHEM.2020.114249.
[58] D. Ledwoch, L. Komsiyska, E.M. Hammer, K. Smith, P.R. Shearing, D.J.L. Brett, E. Kendrick, Determining the electrochemical transport parameters of sodium-ions in hard carbon composite electrodes, Electrochim. Acta 401 (2022) 139481, https://doi.org/10.1016/J.ELECTACTA.2021.139481.
[59] B. Campbell, R. Ionescu, Z. Favors, C.S. Ozkan, M. Ozkan, Bio-derived, binderless, hierarchically porous carbon anodes for Li-ion batteries, Sci. Rep. 5 (2015) 14575, https://doi.org/10.1038/srep14575.
[60] H.S. Hirsh, B. Sayahpour, A. Shen, W. Li, B. Lu, E. Zhao, M. Zhang, Y.S. Meng, Role of electrolyte in stabilizing hard carbon as an anode for rechargeable sodium-ion batteries with long cycle life, Energy Storage Mater. 42 (2021) 78–87, https://doi.org/10.1016/J.ENSM.2021.07.021.
[61] J. Pan, Y.Y. Sun, Y. Yan, L. Feng, Y. Zhang, A. Lin, F. Huang, J. Yang, Revisit electrolyte chemistry of hard carbon in ether for Na storage, JACS Au 1 (2021) 1208–1216, https://doi.org/10.1021/jacsau.1c00158.
[62] Y. Li, F. Wu, Y. Li, M. Liu, X. Feng, Y. Bai, C. Wu, Ether-based electrolytes for sodium ion batteries, Chem. Soc. Rev. 51 (2022) 4484–4536, https://doi.org/10.1039/D1CS00948F.
[63] H. Alptekin, H. Au, E. Olsson, J. Cottom, A.C.S. Jensen, T.F. Headen, Q. Cai, A. J. Drew, M. Crespo Ribadeneyra, M.M. Titirici, Elucidation of the solid electrolyte interphase formation mechanism in micro-mesoporous hard-carbon anodes, Adv. Mater. Interfac. 9 (2022) 2101267, https://doi.org/10.1002/ADMI.202101267.
[64] H. Au, N. Rubio, D.J. Buckley, C. Mattevi, M.S.P. Shaffer, Thermal decomposition of ternary sodium graphite intercalation compounds, Chem. Eur J. 26 (2020) 6545–6553, https://doi.org/10.1002/CHEM.202000422.